RESEARCH

Plasmonic Sensor Based on S-Shaped Metal-Insulator-Metal Waveguide for the Detection of Water-Soluble Vitamins

Yiping Sun[1] · Yongpeng Ren[1] · Desheng Qu[1] · Fumeng Qin[1] · Chunlei Li[1]

Abstract

In this study, a compact plasmonic sensor that can generate dual Fano resonances is proposed. The structure is composed of a metal-insulator-metal (MIM) S-shaped waveguide with baffle, an analogous C-shaped resonator (ACR), and a T-shaped resonator with an annular cavity (TRAC). Employing the finite element method (FEM), the optical transmission characteristics of the structure are investigated. The results indicate that the dual Fano resonances arise from different resonators and can be independently tuned by altering the structural parameters of different resonators. Then, through adjusting the refractive index (RI) of the medium within the resonator in the range of 1.3–1.4, the RI sensing properties of the structure are also analyzed. The maximum RI sensitivity (*S*) and figure of merit (*FOM*) can be up to 2400 nm/RIU and 95.86 RIU^{-1}. Moreover, depending on the independence of the ACR and the TRAC, the sensor has efficient biochemical sensing characteristics and is used to achieve simultaneous determination of water-soluble vitamin B1 and vitamin C. The corresponding concentration sensitivities can be up to 500 nm·ml/g and 224 nm/C_{vc}, respectively. Consequently, the structure has significant potential for multifunctional biochemical sensing applications in high-density integrated circuits.

Keywords Plasmonic sensor · MIM · Fano resonance · Independent tunability · Water-soluble vitamins

Introduction

Surface plasmon polaritons (SPPs) are electromagnetic (EM) waves excited through the interaction of incident photons and the free electrons in metals, which propagate along the metal-insulator interface [1]. In addition, their amplitudes decrease exponentially along perpendicular to the metal-insulator surface [2]. The EM energy is strongly localized near the boundary, which enables to break through the conventional optical diffraction limit and to manipulate light in sub-wavelength scales [3]. Therefore, SPPs have received attentions from many researchers, and numerous photonic devices with different functions have been designed and examined, such as plasmonic sensors, absorbers, filters, switches, and slow light devices [4–8]. Among them, plasmonic sensing has become an important area of biosensing research due to its label-free detection, fast response, and strong resistance to EM interference [9]. So far, most of

the plasmonic sensors are usually realized based on metal-insulator-metal (MIM) waveguide coupled cavity resonators [10]. The main advantages of MIM waveguide structures are low fabrication cost, high ability to confine light, simple structure, easy integration, and low bending loss [11]. Hence, MIM waveguide structures are considered to be one of the most desirable methods for realizing nano-integrated photonic devices.

MIM waveguide structures based on SPPs can arise many unique optical phenomena, such as Fano resonance and plasma-induced transparency (PIT) [12, 13]. Fano resonance, possessing a sharp and asymmetric line shape in the transmission spectrum, is widely used in the field of plasmonic sensing because of its highly sensitive properties to structural parameters and ambient environment [14]. It can be achieved through the mutual interference of a wide continuous state and a narrow discrete state. In recent years, many works have been published with respect to plasmonic sensors based on MIM waveguide by utilizing multiple Fano resonances. Qi et al. designed a stub MIM straight waveguide coupled to an elliptical ring resonator. The structure can excite triple Fano resonances and obtain a refractive index (RI) sensitivity of 1400 nm/RIU [15]. Yadav et al.

✉ Chunlei Li
  licl915@163.com

[1] College of Science, Northeast Forestry University, Harbin 150040, Heilongjiang, China

proposed a plasmonic sensor based on a MIM straight waveguide coupled tapered waveguide cavity resonator. It was able to excite dual Fano resonances and obtain the highest RI sensitivity up to 2544.3 RIU/nm [16]. Figuigue et al. studied an MIM waveguide system consisting of a semi-elliptical ring and a MIM straight waveguide with baffle. The system can generate triple Fano resonances and achieve a RI sensitivity 1783 RIU/nm and a figure of merit (*FOM*) of 27 [17]. Multiple Fano resonances often originate from the common resonator, which restricts the flexibility of plasmonic sensor. Therefore, Liu et al. reported the independent tunability of multiple Fano resonances using a MIM straight waveguide with baffle coupling two resonators (a rectangular resonator and a semicircular ring resonator) [18]. However, for MIM straight waveguide coupling multiple resonators, this approach reduces the usage efficiency for the integration space. To further enhance the integration of photonic devices, MIM S-shaped waveguides exhibit higher practical value. At present, there are fewer studies based on MIM S-shaped waveguide coupling to achieve the independent tunability of plasmonic sensors. Moreover, the sensing performances of plasmonic structures should be also further improved.

In this work, a compact plasmonic sensor consisting of a MIM S-shaped waveguide with baffle, an analogous C-shaped resonator (ACR), and a T-shaped resonator with an annular cavity (TRAC) is proposed. The transmission spectrum and magnetic field distribution are numerically simulated through the finite element method (FEM). The impacts of structural parameters on Fano resonances are investigated, and independent tunability of multiple Fano resonances can be realized by adjusting the structural parameters of different resonators. Finally, the plasmonic sensor is explored for the simultaneous determination of two water-soluble vitamins.

Structure design and theoretical analysis

We design a simple and compact plasmonic sensor structure which is comprised of a MIM S-shaped waveguide with baffle, an analogous C-shaped resonator (ACR), and a T-shaped resonator with an annular cavity (TRAC), as illustrated in Fig. 1. Silver and gold are broadly employed for RI sensing among all plasmonic materials [19, 20], while the silver is chosen as a metallic material which is mainly attributed to its cheaper and low-loss properties [21]. For the easy oxidation of silver, it can be covered with a thin layer of silica to avoid direct contact with air [22]. The orange and white areas represent metallic silver and air, respectively. To ensure that only the fundamental transverse-magnetic (TM$_0$) mode is transmitted in the waveguide structure, the widths of both the S-shaped
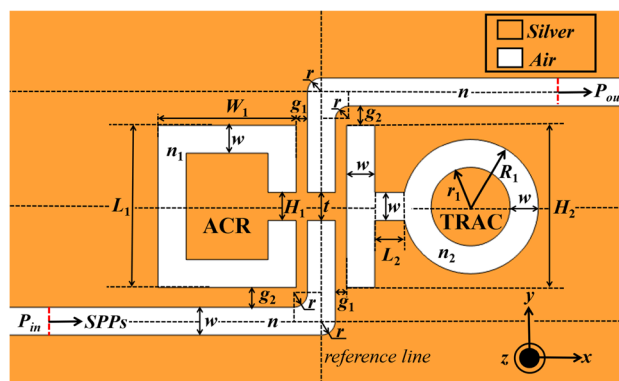

Fig. 1 Schematic diagram of the plasmonic sensor structure

waveguide and the resonators are fixed to $w = 50$ nm, and the radius of the arc at the bend is fixed to $r = 25$ nm [23]. For the S-shaped waveguide, the ACR and the TRAC are situated on its left and right sides, and the coupling distances in the x and y directions are represented by g_1 and g_2, respectively. Moreover, the thickness of baffle in the waveguide is defined as t. The ACR can be considered as one rectangular ring with a gap. The length and width of the rectangular ring and the height of the gap are indicated by L_1, W_1, and H_1, respectively. Similarly, the TRAC can be also disassembled into one big rectangle, one connected gap and one ring. The lengths of the big rectangle and the connected gap are H_2 and L_2, while the inner and outer radii of the ring are denoted by R_1 and r_1, respectively. In addition, the refractive indices (RIs) of the medium materials within the MIM waveguide, ACR, and TRAC are defined as n, n_1, and n_2, respectively. Then, the plasmonic sensor structure is constructed and simulated employing the finite element method (FEM). Since the calculation results of 2D model and 3D model are almost identical when the thickness in the z direction is out of 1 μm [24]. Thus, to boost calculation efficiency, all structures are calculated based on the 2D model.

In the simulation process, SPPs are passed from the left input port to the right output port of the MIM waveguide, and the powers (P_{in} and P_{out}) at the input and output ports are examined. Thereby, the transmittance (T) is able to be calculated by $T = P_{out}/P_{in}$. Additionally, two mode couplers can be integrated into the ports of S-shaped waveguide, respectively. They can effectively contribute to convert between dielectric mode and plasmonic mode [25, 26]. To absorb the escaping electromagnetic (EM) waves, we set up perfect matching layers around the simulation area. The permittivity of air is $\varepsilon_i = 1.0$. Silver, as a metallic material, exhibits a relative permittivity (ε_m) as a function of frequency and can be described by the classic Drude model [27]:

$$\varepsilon_m(\omega) = \varepsilon_\infty - \frac{\omega_p^2}{\omega(\omega + i\gamma)}, \tag{1}$$

where ω represents the angular frequency of incident photons, while parameters γ, ω_p, and ε_∞ are the damping attenuation frequency, the plasmonic resonance frequency, and the permittivity at infinite frequency, respectively. And the values of these parameters for silver are set to $\gamma = 2.73 \times 10^{13}$ rad/s, $\omega_p = 1.38 \times 10^{16}$ rad/s, and $\varepsilon_\infty = 3.7$. Since the waveguide width is much smaller than the wavelength of the incident light, only the TM_0 mode is propagated in the waveguide. The dispersion equation of TM_0 mode in the waveguide can be given as follows [28]:

$$\tanh\left(\frac{w\sqrt{\beta^2 - \varepsilon_i k_0^2}}{2}\right) + \frac{\varepsilon_i \sqrt{\beta^2 - \varepsilon_m k_0^2}}{\varepsilon_m \sqrt{\beta^2 - \varepsilon_i k_0^2}} = 0, \tag{2}$$

Here, $k_0 = 2\pi/\lambda_0$ and β are the wave vectors of SPPs in free space and in MIM waveguide. Thus, the effective RI (n_{eff}) is described as $n_{\text{eff}} = \beta/k_0$. Then based on the standing wave theory, the resonance is excited when the wavelength of incident light satisfies the phase matching condition of resonator. And the resonance wavelength (λ_{res}) can be represented as [29]

$$\lambda_{res} = \frac{2L_{eff}\text{Re}(n_{eff})}{m - \frac{\varphi_{ref}}{\pi}}, \tag{3}$$

where L_{eff} is the effective length of resonator, $\text{Re}(n_{eff})$ is the real part of effective RI, and φ_{ref} is the reflection phase shift of SPPs. The positive integer m indicates the order of resonance.

Generally, for the sensing properties of plasmonic sensors, sensitivity (S) and figure of merit (FOM) are two important evaluation parameters, and they can be calculated by the following equations, respectively [30].

$$S = \frac{\Delta\lambda_{res}}{\Delta n}, \tag{4}$$

$$FOM = \frac{\Delta T}{T\Delta n}, \tag{5}$$

Here, Δn is the RI change, while $\Delta\lambda_{res}$ and ΔT are the corresponding changes in the resonance wavelength and the transmittance.

Numerical results and discussion

The default parameter settings are listed in Table 1. So far, electron beam lithography (EBL), nano-imprint lithography (NIL), and focused ion beam (FIB) lithography are commonly employed to fabricate nanoscale photonic devices [31]. Among them, EBL with sub-10 nm resolution can satisfy the required accuracy of the designed structure [32]. Firstly, a silver layer with sufficient thickness is deposited on the Si substrate utilizing the magnetron sputtering method. Subsequently, the silver layer is covered with a polymethyl methacrylate resist, and the desired pattern is created on its surface using an electron beam. The exposed areas undergo chemical development and silver etching, followed by removal of the resist from the surface.

To study the optical properties of the proposed plasmonic sensor, the transmission spectra of sensor structure without resonators, sensor structure without baffle, and the whole structure are numerically simulated and displayed in Fig. 2a. According to the formation conditions of Fano resonance, it can be seen from the black dashed line in Fig. 2a that the sensor structure without resonator generates a continuous spectrum with low transmittance. Whereas for the spectrum of the sensor structure without baffle, the red dashed line exhibits two narrow discrete states. Therefore, the whole structure is capable of exciting the dual Fano resonances (FR_1 and FR_2), as seen in the blue solid line. Moreover, the simulated values are verified by matching the transmission spectra to the Fano profile (FP). The theoretical FP values can be obtained by Fano liner equation [33]:

$$F(\lambda) = \frac{A(q + b)}{(1 + b^2)}, b = \frac{(\frac{1}{\lambda} - \frac{1}{\lambda_{res}})\lambda_{res}^2}{\Delta\lambda}. \tag{6}$$

where q is Fano factor. A and $\Delta\lambda$ stand for the amplitude and linewidth of Fano resonance. The FP values of FR_2 and

Table 1 Summary of the default parameter settings

Illustration	Symbol	Value	Unit
The widths of waveguide and resonators	w	50	nm
The thickness of baffle	t	50	nm
The arc radius at waveguide bend	r	25	nm
RI of medium in waveguide	n	1	-
The coupling distances of resonators	g_1	10	nm
	g_2	35	nm
The length of the rectangular ring in ACR	L_1	290	nm
The width of the rectangular ring in ACR	W_1	220	nm
The height of gap in ACR	H_1	50	nm
RI of medium in ACR	n_1	1	-
The outer radius of ring in TRAC	R_1	120	nm
The inner radius of ring in TRAC	r_1	R_1-w	nm
The length of the connected gap in TRAC	L_2	50	nm
The length of the big rectangle in TRAC	H_2	290	nm
RI of medium in TRAC	n_2	1	-

Fig. 2 **a** Transmission spectra: sensor structure without resonators (black dashed line), sensor structure without baffle (red dashed line), and whole structure (blue solid line). **b** FEM and FP curves for FR_2. **c** FEM and FP curves for FR_1
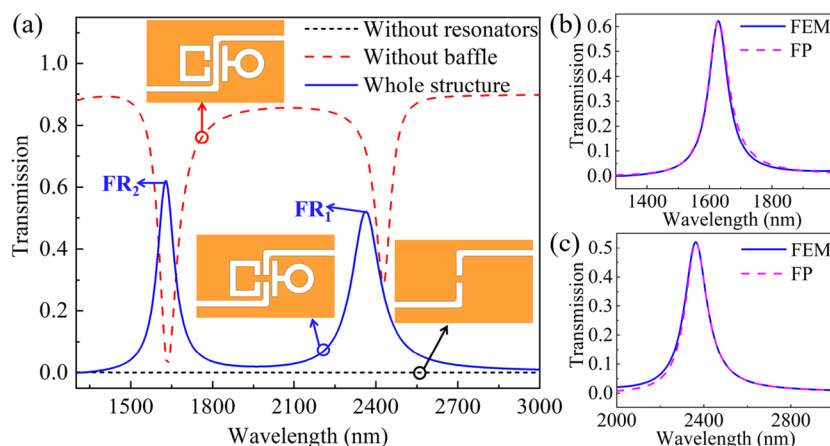

FR_1 are fitted, as depicted in Fig. 2b and c. The q values for FR_2 and FR_1 are calculated to be -56.9765 and -56.7682, respectively. It can be seen that there is a great agreement between the FEM simulated values and the FP fitted values. Then, to further investigate the formation mechanism of FR_1 and FR_2, the transmission spectra of the structures with different resonators and the distributions of magnetic fields at FR_1 and FR_2 are also analyzed, as presented in Fig. 3. It can be seen that FR_1 can be excited only when the ACR exists. Similarly, FR_2 can be excited only when the TRAC is present. Combining with the magnetic field distributions at the corresponding resonance wavelengths, the energy at FR_1 is primarily concentrated in the ACR, and the energy at FR_2 is mainly focused in the TRAC. In addition, both of them keep high transmittance at the P_{out}. As a result, it can

be indicated that FR_1 and FR_2 originate from the ACR and the TRAC, respectively.

Next, the effects of structural parameters on the Fano resonances are explored. In Fig. 4a, the gap height H_1 in the ACR is increased from 50 to 90 nm, with an increment of 10 nm. Other structural parameters are kept at the default settings. It can be observed that with the increase of H_1, the FR_1 exhibits a significant blueshift and accompanies a decrease in transmittance, whereas the FR_2 remains unchanged. The reason for this phenomenon is that the reduction of H_1 is equivalent to decreasing the effective length of the ACR. Based on Eq. (3), it is known that the diminishment of the effective length results in the reduction of the resonance wavelength; thereby, the FR_1 exhibits a blueshift. Moreover, the increase in the gap height reduces the coupling length between the

Fig. 3 **a** The transmission spectra of only ACR, only TRAC, and the whole structure. The distributions of magnetic fields: **b** FR_2, **c** FR_1
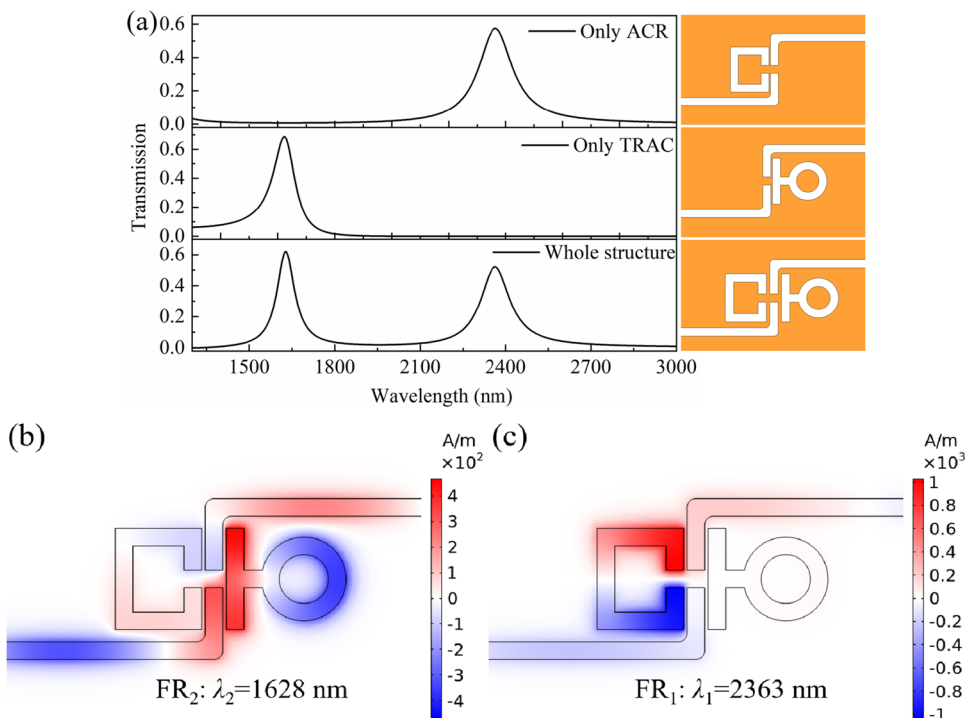
Fig. 4 **a** The transmission spectra of the structures with different parameters H_1. **b** The linear fitting of the resonance wavelength with H_1
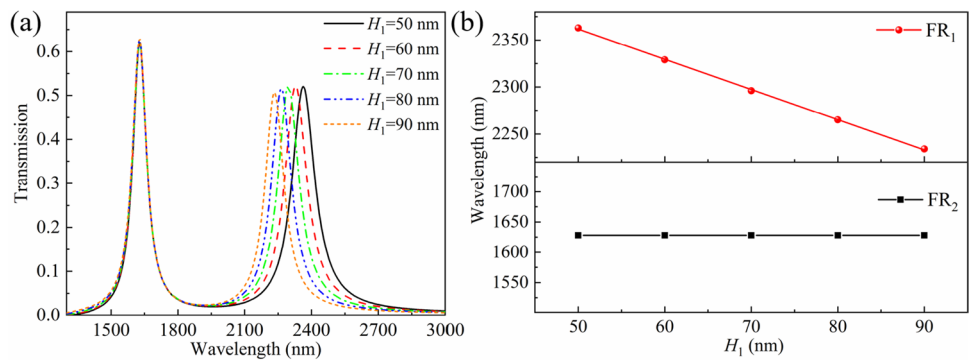

ACR and the S-shaped waveguide, which leads to a decrease in the transmittance of FR_1. And from Fig. 4b, it can be found that there is a good linear relationship between the resonance wavelength of FR_1 and H_1, which has a linearity as high as 0.99954. Conversely, the length H_2 of the big rectangle in the TRAC is decreased from 290 to 250 nm with an interval of 10 nm, as depicted in Fig. 5a. Other structural parameters are also maintained as the default settings. In this case, the resonance wavelength of FR_2 exhibits a blueshift with the decrease of H_2 and that of FR_1 remains unchanged. The transmittance of FR_2 also exhibits a slight decrease. The reason for this is consistent with the effect of H_1 on FR_1. It can also be noticed from Fig. 5b that the resonant wavelength of FR_2 has an excellent linear relationship with H_2 and the linearity reaches 0.99963. Therefore, the resonance wavelengths of FR_1 and FR_2 can be independently controlled by varying the corresponding structural parameters H_1 and H_2, respectively. Namely, the independent tuning of double Fano resonances can be realized.

When the RI of filled medium in the resonator is changed, the resonance wavelength of Fano resonance is also affected and exhibits extreme sensitivity. Thus, this mechanism is widely used in the study of RI sensing. In Fig. 6, by changing the RI (n_1 or n_2) of the medium within the different resonators, only the resonance wavelength of corresponding Fano resonance can be changed. This indicates that independent tunability of the FR_1 and the FR_2

can also be achieved by changing the RI of medium within different resonators. Then, since we expect the designed plasmonic sensor to be used for concentration determination in water-based solutions, we further investigate the sensing properties of the proposed structure, and the RIs ($n_1 = n_2$) of the mediums within the two resonators are regulated between 1.3 and 1.4, as shown in Fig. 7. As the RIs increase, both FR_1 and FR_2 show an obvious redshift and a decrease in transmittance. The RI and dielectric constant of the medium are positively correlated. Based on Eqs. (2) and (3), the increased dielectric constant leads to an increase in the effective RI within the resonator, which causes the resonant wavelength to exhibit a redshift. Moreover, the increase of effective RI also enhances the energy loss of SPPs, which leads to the decrease of transmittance. Figure 7b presents the linear fitting between the resonance wavelength and RI. According to Eq. (4), it is known that the slope of the fitting straight line represents the sensitivity of the corresponding resonance. Therefore, the sensitivities of FR_1 and FR_2 are 2400 nm/RIU and 1650 nm/RIU, respectively. Meanwhile, based on Eq. (5), we can obtain the *FOM* curve of the designed sensor, as shown in Fig. 8. It can be observed that there is a maximum *FOM* value of 95.86 RIU^{-1} at 2302 nm. Table 2 lists the performance comparison of this study with other published works in recent years. It can be demonstrated that the plasmonic sensor structure has favorable sensing characteristics.
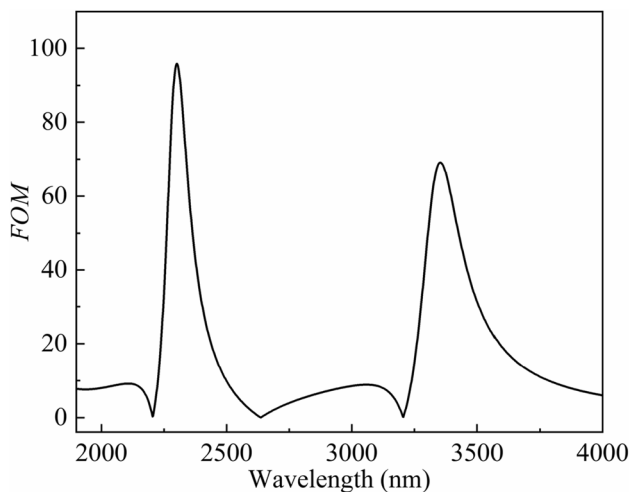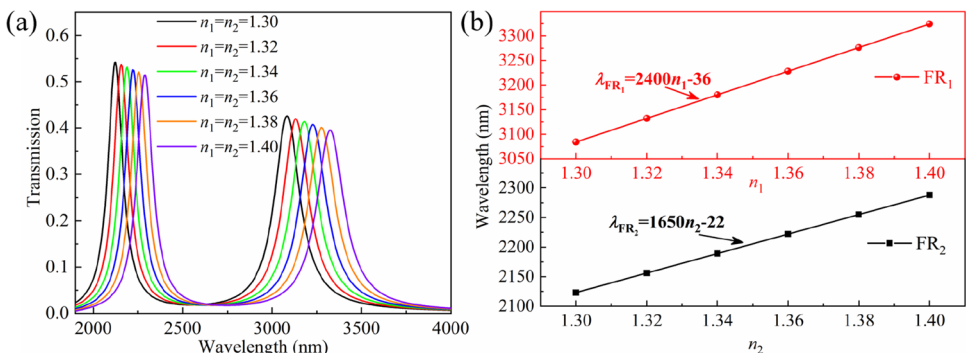
Fig. 5 **a** The transmission spectra of the structures with different parameters H_2. **b** The linear fitting of the resonance wavelength with H_2
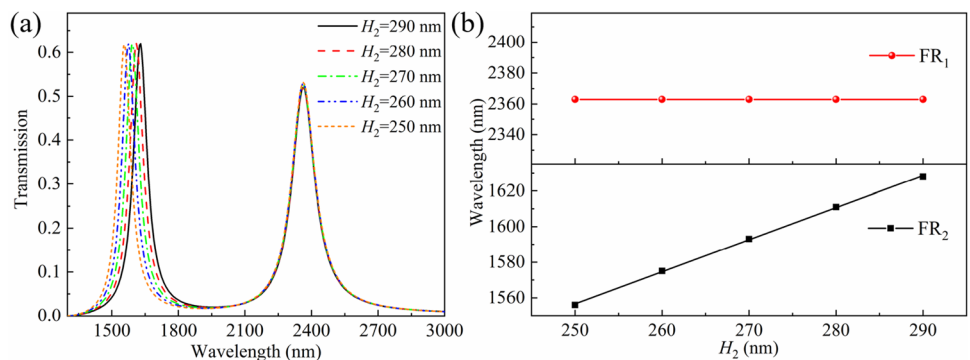
Fig. 6 **a** The transmission spectra of different RI n_1 in ACR. **b** The transmission spectra of different RI n_2 in TRAC
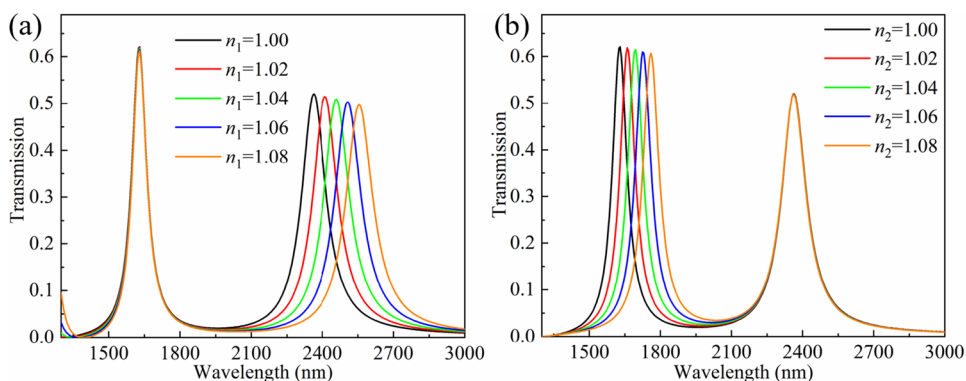
Fig. 7 **a** The transmission spectra of different RIs ($n_1 = n_2$) in resonators. **b** The linear fitting of the resonance wavelength and RIs

Fig. 8 The *FOM* curve of the designed sensor

Table 2 Performance comparison with other published works

| Reference	S (nm/RIU)	FOM_{max} (RIU^{-1})	Year
[34]	1070	-	2020
[35]	1074.88	32.4	2021
[36]	2260	56.5	2021
[37]	1007.78	29	2022
[38]	2280	76.7	2022
[39]	1481	87.3	2023
[40]	1132.14	48.17	2023
[41]	1250	54	2024
[42]	2300	60	2024
This study	2400	95.86	-

Application

Upon the above conclusions, the double Fano resonances excited in this sensor are independently tunable. Therefore, it can be used for the simultaneous determination of two substances, which will greatly improve its efficiency in practical applications. At present, plasmonic sensors are often employed for the detection of bio-chemical analytes, such as glucose, blood samples, and glycerol [43–45]. Vitamins are a category of organic substances that are indispensable for the support of normal physiological activity in humans and animals. Most of them cannot be produced by the organism themselves and must be obtained from food [46]. In particular, the intake of vitamin B1 can effectively improve diseases such as indigestion and neuritis, but too much intake can also lead to metabolic abnormalities and even induce toxic symptoms. The injection of vitamin C can be an effective treatment for scurvy and play an adjunctive role in the treatment of some chronic diseases [47]. Nonetheless, excessive injections can also lead to pro-coagulation of red blood cells
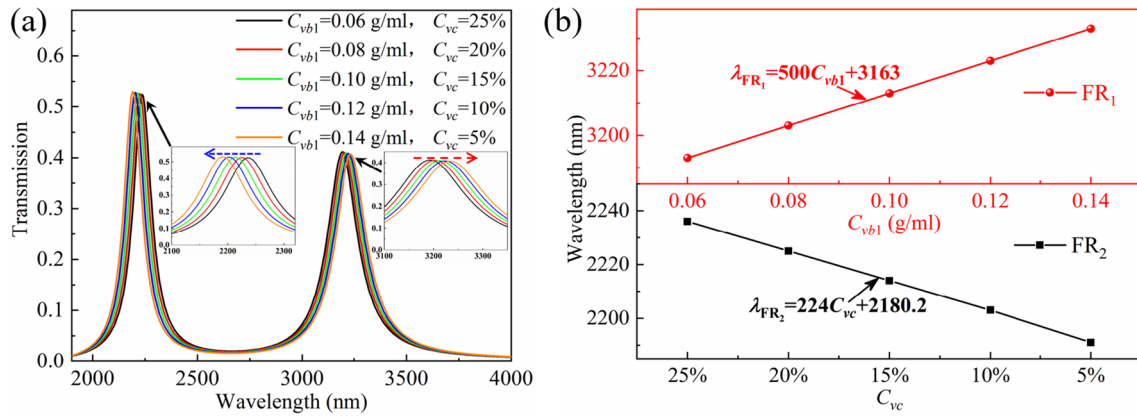
Fig. 9 a The transmission spectra: water-soluble vitamin B1 (ranging from 0.06 to 0.14 g/ml) and water-soluble vitamin C (ranging from 25 to 5%). **b** The linear fitting of the resonance wavelength and the concentration of water-soluble vitamin

and increase the formation of thrombosis in the body [48]. Therefore, the precise measurement of their concentration is extremely significant in the medical field. Here, based on the plasmonic sensor designed in this study, the simultaneous measurement of two water-soluble vitamins (vitamin B1 and vitamin C) is discussed. At room temperature, the mathematical relationships between the RIs of vitamin B1 and vitamin C with respect to concentration are given below [49, 50].

$$n_b = 0.208607 C_{vb1} + 1.33281, \tag{7}$$

$$n_c = 0.13596 C_{vc} + 1.33480, \tag{8}$$

where n_b and C_{vb1} (g/ml) represent the RI and concentration of water-soluble vitamin B1. Similarly, n_c and C_{vc} (%) are the RI and concentration of water-soluble vitamin C. Then, water-soluble vitamin B1 and vitamin C are filled into the ACR and the TRAC as the sensing mediators, respectively. As shown in Fig. 9a, the concentration C_{vb1} of water-soluble vitamin B1 in the ACR is increased from 0.06 to 0.14 g/ml with a step of 0.02 g/ml. Meanwhile, the concentration C_{vc} of water-soluble vitamin C in the TRAC is decreased from 25 to 5% with an interval of 5%. It can be seen that FR$_1$ exhibits redshift, while FR$_2$ exhibits blueshift. This is also further validated the independence between the ACR and the TRAC. Figure 9b shows the linear fitting between the resonance wavelength and the concentration of the water-soluble vitamin. According to Eq. 4, the concentration sensitivity for the water-based solutions can be defined as $S' = \Delta\lambda_{res}/\Delta C$. Thus, with respect to the sensing of water-soluble vitamin B1 and vitamin C, the concentration sensitivities of FR$_1$ and FR$_2$ are as high as 500 nm·ml/g and 224 nm/C_{vc}, respectively. These results indicate that proposed plasmonic sensor structure can efficiently accomplish simultaneous measurements of water-soluble vitamin B1 and vitamin C.

Conclusion

In summary, we design a plasmonic sensor structure that is consisted of a MIM S-shaped waveguide with baffle, an ACR, and a TRAC. Using the FEM, the transmission spectrum and magnetic fields of the sensor structure are simulated and analyzed. The structure is able to excite two Fano resonances which originate from different resonators. The independent tunability of the dual Fano resonances can be achieved by changing the structural parameters H_1 and H_2, while the linearities are as high as 0.99954 and 0.99963, respectively. Similarly, by varying the refractive index of the medium in different resonators, the Fano resonances can be also tuned independently, which greatly increases the flexibility of the plasmonic sensor. Then, based on the RI range of water-based solutions, the sensing properties of the structure are researched. The results show that the designed structure can obtain a maximum sensitivity of 2400 nm/RIU and *FOM* of 95.86 RIU^{-1}. Furthermore, due to the independence of the dual Fano resonances, the plasmonic sensor enables simultaneous determination of water-soluble vitamin B1 (FR$_1$) and vitamin C (FR$_2$) and exhibits concentration sensitivities of 500 nm·ml/g and 224 nm/C_{vc}, respectively. These findings will provide valuable references for the exploitation of nanophotonic devices and high-density integrated circuits.

Declarations

Ethics Approval This manuscript was created entirely by the authors and was never before published. There are no plans to publish this work elsewhere at the moment. The work accurately and thoroughly reflects the authors' own research and analysis. Neither humans nor animals were involved in this study.

Competing Interests The authors declare no competing interests.

5. References

1. Zhang XY, Yan SB, Chen ZB, Ren YF, Zhang Y, Liu PW, Shen LF, Li TS (2022) Refractive index sensor based on a ring with a disk-shaped cavity or temperature detection applications. Appl Optics 61(14):3997–4004
2. Butt MA, Khonina SN, Kazanskiy NL (2022) Simple and improved plasmonic sensor configuration established on MIM waveguide for enhanced sensing performance. Plasmonics 17(3):1305–1314
3. Zhang YJ, Kuang YQ, Zhang ZD, Tang Y, Han JQ, Wang RB, Cui JG, Hou YL, Liu WY (2019) High-sensitivity refractive index sensors based on Fano resonance in the plasmonic system of splitting ring cavity-coupled MIM waveguide with tooth cavity. Appl Phys A-Mater Sci Process 125(1):5
4. Chen F, Yang WX (2022) Pressure sensor based on multiple Fano resonance in metal-insulator-metal waveguide coupled resonator structure. J Opt Soc Am B-Opt Phys 39(7):1716–1722
5. Ebadi SM, Khani S (2023) Design of a tetra-band MIM plasmonic absorber based on triangular arrays in an ultra-compact MIM waveguide. Opt Quantum Electron 55(6):16
6. Liu C, Zhang JY, Feng HL, Fang DC, Wang JC, Wang LH, Zhang ZX, Gao Y (2022) Bifunctional MIM device with narrowband filtering and high-performance sensing. Micro Nanostructures 169:7
7. Dehghan M, Moravvej-Farshi MK, Ghaffari-Miab M, Jabbari M, Darvish G (2019) Ultra-compact spatial terahertz switch based on graphene plasmonic-coupled waveguide. Plasmonics 14(6):1335–1345
8. Chen F, Yang WX (2023) Nanosensor and slow light based on quintuple Fano resonances in a metal-insulator-metal waveguide coupled with a concentric-ring resonator. J Opt Soc Am B-Opt Phys 40(4):736–742
9. Yadav GK, Metya SK (2023) Plasmonic nanosensor for cancer cell detection with multi Fano resonance. Plasmonics 18(3):1195–1202
10. Hocini A, Ben Salah H, Khedrouche D, Melouki N (2020) A high-sensitive sensor and band-stop filter based on intersected double ring resonators in metal-insulator-metal structure. Opt Quantum Electron. 52(7):10
11. Sun YP, Qu DS, Ren YP, Li CL (2024) Nanorods-enhanced MIM plasmonic sensor based on S-shaped waveguide coupled with ohm-shaped and D-shaped resonators. Physica E 161:9
12. Khani S, Afsahi M (2023) Optical refractive index sensors based on plasmon-induced transparency phenomenon in a plasmonic waveguide coupled to stub and nano-disk resonators. Plasmonics 18(1):255–270
13. Yan SB, Yang XY, Xu DJ, Su H, Wu XS, Hua ET (2021) MIM structure with inverted m-type cavity for sensing applications. IEEE Sens J 21(6):7468–7477
14. Zhu J, Yin JG, Li N, Qin YB (2022) Novel glucose concentration sensor with unique resonance lineshapes in optical cavity. Measurement 194:7
15. Qi YP, Chen HW, Zhao SY, Wen YJ, Wang XX (2022) Tunable plasmon refractive index sensor and slow light characteristics based on a stub coupled with an ellipse resonator and its derived structure. J Opt Soc Am B-Opt Phys 39(11):2957–2968
16. Yadav GK, Metya SK (2024) Fano-resonance-based plasmonic refractive index sensor with high sensitivity for detection of urea. J Opt Soc Am B: Opt Phys 41(1):175–185
17. Figuigue M, Mahboub O, El Haffar R (2024) Optical properties of multiple fano resonance in MIM waveguide system coupled with a semi-elliptical ring resonator. Plasmonics 19(2):721–732
18. Liu X, Li JN, Chen JF, Rohimah S, Tian H, Wang JF (2021) Independently tunable triple Fano resonances based on MIM waveguide structure with a semi-ring cavity and its sensing characteristics. Opt Express 29(13):20829–20838
19. Kazanskiy NL, Khonina SN, Butt MA (2020) Plasmonic sensors based on Metal-insulator-metal waveguides for refractive index sensing applications: a brief review. Physica E 117:10
20. Rashid KS, Tathfif I, Yaseer AA, Hassan MF, Sagor RH (2021) Cog-shaped refractive index sensor embedded with gold nanorods for temperature sensing of multiple analytes. Opt Express 29(23):37541–37554
21. Tathfif I, Hassan MF, Rashid KS, Yaseer AA, Sagor RH (2022) A highly sensitive plasmonic refractive index sensor based on concentric triple ring resonator for cancer biomarker and chemical concentration detection. Opt Commun 519:12
22. Jumat S, Chao CTC, Chau YFC, Mahadi AH, Kooh MRR, Kumara N, Chiang HP (2021) Plasmonic refractive index sensor based on the combination of rectangular and circular resonators including baffles. Chin J Phys 71:286–299
23. Zhang ZJ, Yang JB, Han YX, He X, Huang J, Chen DB (2020) Direct coupling strategy in plasmonic nanocircuits for low loss and easy fabrication. Plasmonics 15(3):761–767
24. Bahramipanah M, Abrishamian MS, Mirtaheri SA, Liu JM (2014) Ultracompact plasmonic loop-stub notch filter and sensor. Sens Actuator B-Chem 194:311–318
25. Butt MA (2024) Plasmonic sensor system embedded with orthogonal mode couplers for simultaneous monitoring of temperature and refractive index. Plasmonics 11. https://doi.org/10.1007/s11468-024-02303-7
26. Butt MA, Piramidowicz R (2024) Orthogonal mode couplers for plasmonic chip based on metal–insulator–metal waveguide for temperature sensing application. Sci Rep 14(1):3474
27. Palizvan P, Olyaee S, Seifouri M (2018) An optical MIM pressure sensor based on a double square ring resonator. Photonic Sens 8(3):242–247
28. Mahbub T, Mahabub-A-Rabbani Q, Mahmud S, Sagor RH (2023) Quintuple grids plasmonic refractive index sensor for organic gas sensing application. Results Phys 51:9
29. Zhang S, Qi YP, Shi Q, Su MR, Zhao SY, Wang XX (2023) Narrow-band notch filter and refractive index sensor based on rectangular-semi-annular cavity coupled with MIM waveguide structure. Phys Scr 98(8):9
30. Qiao LT, Zhang GM, Wang ZS, Fan GP, Yan YF (2019) Study on the Fano resonance of coupling M-type cavity based on surface plasmon polaritons. Opt Commun 433:144–149
31. Hassan MF, Sagor RH, Tathfif I, Rashid KS, Radoan M (2021) An Optimized Dielectric-Metal-Dielectric Refractive Index Nanosensor. IEEE Sens J 21(2):1461–1469
32. Tathfif I, Yaseer AA, Rashid KS, Sagor RH (2021) Metal-insulator-metal waveguide-based optical pressure sensor embedded with arrays of silver nanorods. Opt Express 29(20):32365–32376
33. Liaw JW, Chen HC, Kuo MK (2013) Plasmonic Fano resonance and dip of Au-SiO$_2$-Au nanomatryoshka. Nanoscale Res Lett 8:1–8
34. Hassan MF, Tathfif I, Radoan M, Sagor RH (2020) A concentric double-ring resonator based plasmonic refractive index sensor

with glucose sensing capability, TENCON 2020 - 2020 IEEE REGION 10 CONFERENCE (TENCON). https://www.ieeexplore.ieee.org/document/9293901

35. Tathfif I, Rashid KS, Yaseer AA, Sagor RH (2021) Alternative material titanium nitride based refractive index sensor embedded with defects: an emerging solution in sensing arena. Results Phys 29:8

36. Liu PW, Yan SB, Ren YF, Zhang XY, Li TS, Wu XS, Shen LF, Hua ET (2021) A MIM waveguide structure of a high-performance refractive index and temperature sensor based on Fano resonance. Appl Sci-Basel 11(22):12

37. Adhikari R, Sbeah Z, Gupta R, Chauhan D, Nunzi JM, Dwivedi RP (2022) Compact and Sensitive H-Shaped Metal-Dielectric-Metal Waveguide Plasmonic Sensor. Plasmonics 17(4):1593–1606

38. Zhou GQ, Yan SB, Chen LL, Zhang XY, Shen LF, Liu PW, Cui Y, Liu JL, Li TS, Ren YF (2022) A nano refractive index sensing structure for monitoring hemoglobin concentration in human body. Nanomaterials 12(21):11

39. Wang LH, Feng HL, Zhang JY, Zhang ZX, Fang DC, Wang JC, Liu C, Gao Y (2023) Surface plasmon polaritons filter with transmission optimized based on the multimode interference coupled mode theory. Plasmonics 18(2):493–502

40. Butt MA, Kazanskiy NL, Khonina SN (2023) Tapered waveguide mode converters for metal-insulator-metal waveguide plasmonic sensors. Measurement 211:7

41. Zhu J, Xu QN, Jian ZH (2024) Novel high performance Fano resonance sensor with circular split ring resonance. Physica B 689:6

42. Cao YH, Yan SB, Liu F, Wang J, Chang SW, Liu G, Zhang W, Wu TQ, Ren YF (2024) A refractive index sensor based on metal-insulator-metal coupling ring resonator with a stub. Front Physics 11:9

43. Li YC, Huang J, Chen F (2023) Quintuple plasmonic fano resonances for the sensing application of glucose concentration and water-soluble vitamins. Plasmonics 18(5):1825–1835

44. Negahdari R, Rafiee E, Emami F (2023) Sensitive biosensors based on plasmonic-graphene nanocombinations for detection of biological elements in blood samples. Plasmonics 18(3):909–919

45. Xu QN, Zhu J (2022) Glycerol concentration sensor based on the MIM waveguide structure. Front Physics 10:9

46. Huang L, Tian SL, Zhao WH, Liu K, Guo JH (2021) Electrochemical vitamin sensors: a critical review. Talanta 222:15

47. Ledford H (2014) Vitamin C injections ease ovarian-cancer treatments. Nature. https://doi.org/10.1038/nature.2014.14673

48. Kim K, Bae ON, Koh SH, Kang S, Lim KM, Noh JY, Shin S, Kim I, Chung JH (2015) High-dose vitamin c injection to cancer patients may promote thrombosis through procoagulant activation of erythrocytes. Toxicol Sci 147(2):350–359

49. Yuan SB, Zhu J, Yin JG (2023) Analysis of the water-soluble vitamins based on MIM waveguide structure and Fano resonance. Heliyon 9(4):11

50. Wu ZB, Zhu J (2024) Characterization of CCTRC waveguide and measurement of vitamin C concentration. Plasmonics 19(2):913–924